

The properties and the formation mechanism of the stellar counter-rotating components in NGC 4191

L. Coccato¹, M. Fabricius^{2,3,4}, L. Morelli^{5,6}, E. M. Corsini^{5,6}, A. Pizzella^{5,6}, P. Erwin^{2,3}, E. Dalla Bontà^{5,6}, R. Saglia^{2,3}, R. Bender^{2,3}, and M. Williams^{2,7}

¹ European Southern Observatory, Karl-Schwarzschild-Straße 2, D-85748 Garching bei München, Germany.

² Max Planck Institute für Extraterrestrische Physik, Giessenbachstraße, D-85748 Garching, Germany.

³ University Observatory Munich, Scheinerstraße 1, 81679 Munich, Germany.

⁴ Subaru Telescope, 650 North Aohoku Place, Hilo, HI 96720.

⁵ Dipartimento di Fisica e Astronomia “G. Galilei”, Università di Padova, vicolo dell’ Osservatorio 3, I-35122 Padova, Italy.

⁶ INAF-Osservatorio Astronomico di Padova, vicolo dell’ Osservatorio 5, I-35122 Padova, Italy.

⁷ Department of Astronomy, Columbia University, New York, NY 10027, USA.

Received April 2015; accepted July 2015

ABSTRACT

Context. Formation of stellar counter-rotating components in galaxies.

Aims. In this paper we disentangle two counter-rotating stellar components in NGC 4191 and characterize their physical properties such as kinematics, size, morphology, age, metallicity, and abundance ratio. NGC 4191 was selected as candidate to host stellar counter-rotating components on the basis of two symmetric peaks in its velocity dispersion two-dimensional map and its irregular velocity field.

Methods. We obtained integral field spectroscopic observations with VIRUS-W and performed a spectroscopic decomposition technique to separate the contribution of two stellar components to the observed galaxy spectrum across the field of view. We also performed a photometric decomposition, modeling the galaxy with a Sérsic bulge and two exponential disks of different scale length, with the aim of associating these structural components with the kinematic components. We then measured the equivalent width of the absorption line indices on the best fit models that represent the kinematic components and compared our measurements to the predictions of stellar population models that account also for variable abundance ratio of α elements.

Results. We have evidence that the line-of-sight velocity distributions (LOSVDs) are bimodal and asymmetric, consistent with the presence of two distinct kinematic components. The combined information of the intensity of the peaks of the LOSVDs and the photometric decomposition allows us to associate the Sérsic bulge and the outer disk with the main kinematic component, and to associate the inner disk with the secondary kinematic component. We find that the two kinematic stellar components counter-rotate with respect to each other. The main component is the most luminous and massive, and it rotates slower than the secondary component, which rotates along the same direction as the ionized gas. The study of the stellar populations reveals that the two kinematic components have the same solar metallicity and sub-solar abundance ratio, without the presence of significant radial gradients. On the other hand, their ages show strong negative gradients and the possible indication that the secondary component is the youngest. We interpret our results in light of recent cosmological simulations and suggest gas accretion along two filaments as the formation mechanism of the stellar counter-rotating components in NGC 4191.

Key words. galaxies: abundances – galaxies: kinematics and dynamics – galaxies: formation – galaxies: stellar content – galaxies: individual: NGC 4191

1. Introduction

The phenomenon of counter-rotation, i.e. the presence of multiple kinematic components that are rotating in opposite directions, has been detected in a number of galaxies of all morphological types (see Corsini 2014 for a review). Counter-rotating galaxies are classed according to the nature of their counter-rotating components, i.e., gas vs. stars (e.g., NGC 4546, Galletta 1987), stars vs. stars (e.g., NGC 4550, Rubin et al. 1992; Rix et al. 1992), and gas vs. gas (e.g., NGC 7332, Fisher et al. 1994). For the cases of stellar counter-rotation, a further classification can be done by looking at the sizes of the decoupled structures. There are galaxies with two counter-rotating stellar disks of similar sizes (e.g., NGC 4550) and galaxies where the

counter-rotation is visible only in the innermost regions (e.g., NGC 448, Krajnović et al. 2011).

Thanks to the advent of integral field spectroscopic surveys like SAURON (de Zeeuw et al. 2002), ATLAS 3D (Cappellari et al. 2011), CALIFA (Sánchez et al. 2012), SAMI (Bryant et al. 2015), and MANGA (Bundy et al. 2015), the census of counter-rotating galaxies has increased. Indeed, these surveys allowed to identify candidate galaxies to host counter-rotating stellar disks by looking for the kinematic signature given by two off-center and symmetric peaks in the stellar velocity dispersion in combination with zero velocity rotation measured along the galaxy major axis. These kinematic features are observed in the radial range where the two counter-rotating components have roughly the same luminosity and their LOSVDs are unresolved (Rix et al. 1992; Bertola et al. 1992; Vergani et al. 2007). Recently, Krajnović et al. (2011) have found 11 galaxies

(including NGC 4191) with a double-peaked velocity dispersion in the volume-limited sample of 260 nearby early-type galaxies gathered by the ATLAS-3D project.

The current paradigm that explains stellar counter-rotation is a retrograde acquisition of external gas and subsequent star formation (Thakar & Ryden 1996; Pizzella et al. 2004; Algorry et al. 2014). Alternative scenarios such as the assembly of the counter-rotating stellar component from mergers (Puerari & Pfenniger 2001; Crocker et al. 2009) or internal instabilities (Evans & Collett 1994) have been proposed, too. The relatively small number of studied cases favors external origin, but it does not yet allow us to distinguish between gas accretion or merging (Coccato et al. 2013; Pizzella et al. 2014).

In order to characterize the physical properties of the two stellar counter-rotating components and therefore to constrain their formation mechanism, we need to disentangle their contribution to the observed galaxy spectrum. To this aim, we introduced a spectral decomposition technique that allows one to measure the kinematics and properties of the stellar populations of the decoupled components (Coccato et al. 2011).

Other parametric (Johnston et al. 2013) and non parametric (Katkov & Chilingarian 2011) techniques have also been proposed and developed by other teams. All these studies show that the stellar component that is rotating along the same direction as the ionized gas is younger, less massive, and has different metallicity and abundance ratio with respect to the main galaxy component. These results are consistent with the gas accretion scenario followed by star formation. We also found that, at least for one case, the small counter-rotation observed in the inner regions is the “tip of the iceberg” of a much larger structure, which is less luminous than the main stellar component and whose real extent can be revealed only by a spectral decomposition (NGC 3593, Coccato et al. 2013).

In this work, we investigate the S0 galaxy NGC 4191, which is an isolated system located at a distance of 42.4 Mpc (Theureau et al. 2007). In contrast to the galaxies we studied in our previous works (Coccato et al. 2011, 2013; Pizzella et al. 2014), NGC 4191 was not already known to host two large-scale counter-rotating stellar disks. We selected NGC 4191 because its stellar velocity field reveals an irregular structure with little rotation, and its stellar velocity dispersion field shows two symmetric peaks located on opposite sides at $\sim 10''$ from the galaxy center along the photometric major axis (Krajnović et al. 2011). The latter feature is one of the key observables proposed for detecting candidate galaxies with stellar counter-rotation. Contrarily to its complex kinematic structure, the photometric profile of NGC 4191 does not reveal prominent sub-structures. The light distribution of NGC 4191 has been modeled with a single Sérsic law with index $n = 2.4$ (Krajnović et al. 2013).

The aim of the paper is to study the structure of NGC 4191 and to investigate the presence of multiple kinematic stellar components. In particular, we want to test whether NGC 4191 does host counter-rotating stellar components and, if present, we want to characterize their kinematics and stellar population properties. Also, we want to investigate whether the kinematic components can be associated with any photometric sub-structure, which might have been overlooked in previous studies. Moreover, if two counter-rotating components are indeed detected, we will have strengthened the case that the presence of a double-peaked signature in the stellar velocity dispersion field combined with the absence of regular rotation can be used as selection criteria for counter-rotating galaxies.

This paper is structured as follows; Section 2 describes the spectroscopic observation and the data reduction; Section 3

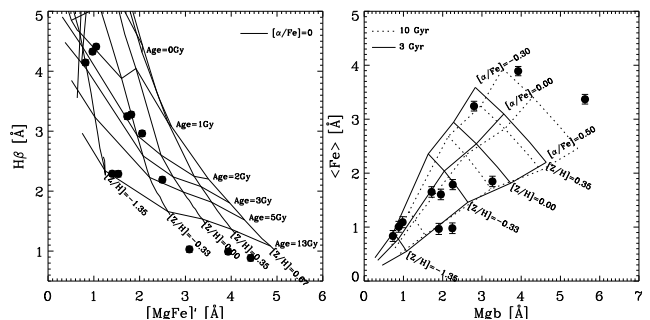


Fig. 1. Location of the observed stars (black dots) in the $[MgFe]'$, $H\beta$ (left panel) and the $Mg\ b$, $\langle Fe \rangle$ (right panel) parameter space. The line grids give the predictions from simple stellar population models by Thomas et al. (2003).

presents our analysis and our results. Finally, we summarize our conclusions in Section 4.

2. Observations and data reduction.

2.1. Observations

The observations of NGC 4191 were carried on 1-3 and 6-7 April 2013 using the VIRUS-W Integral Field Unit (IFU) Spectrograph (Fabricius et al. 2012) at the 2.7-m Harlan J. Smith Telescope of the McDonald Observatory (Texas, US). The IFU consists of 267 fibres arranged in a rectangular grid, which covers a field of view $105'' \times 55''$ with a fill factor of 1/3. Each fibre has a diameter of $3''.2$ on the sky. We used the lower resolution mode of the instrument which covers the $4340\text{\AA} - 6040\text{\AA}$ wavelength range with a spectral resolution of 1.57\AA FWHM ($\sigma_{\text{instr}} \sim 38\text{ km s}^{-1}$)¹.

The observations were dithered to fill the entire field of view. We took 6 exposures of 1800 sec in each of the three dither positions and bracketed and interleaved them with 300 sec sky nods. Each of the science exposures was split in two for cosmic ray rejection. The total on-target exposure time per fibre is 3 h. We recorded bias frames and Hg+Ne arc lamp exposures for wavelength calibration on the evenings and mornings before and after the observations. We also recorded dome flat exposures to trace the fibre positions on the detector and to compensate for fibre-to-fibre throughput variation. A set of spectroscopic standard stars were also observed with the same instrumental set-up.

2.2. Data reduction

The data reduction follows the same methodology as described in Fabricius et al. (2014). In short, after subtraction of the master bias the fiber positions are traced by searching along the peaks of the spectra in the dome flat frames. Then the arc peak positions are identified in the master arc frames by searching along those traces. The fiber/wavelength to x/y pixel position mapping is then modeled and fit — using a standard least squares minimization routine — with a two-dimensional 7-th degree Chebyshev polynomial. We use 28 Hg and Ne spectral lines for the fit.

After the wavelength calibration we average the two cosmic ray split science exposures as well as the bracketing sky frames

¹ The spectral resolution of VIRUS-W below 4800\AA deteriorates up to $\sigma_{\text{instr}} \sim 70\text{ km s}^{-1}$. We tested that restricting the wavelength range to $4800\text{\AA} - 6040\text{\AA}$ has negligible effects on our results.

while rejecting spurious events using the `PyCosmic` routine (Husemann et al. 2012). We extract science, sky and dome-flat spectra by stepping along the previously determined trace positions. For each step, the counts in the CCD pixels are assigned to spectral pixels according to the areal overlap of the CCD pixel with the 7 pixel wide and 0.52 \AA long extraction aperture. We correct for fiber-to-fiber throughput variations using the extracted dome-flat spectra and remove the sky background by scaling the sky spectra by the relative exposure time.

Then, we combine all flat-fielded and background-removed science spectra into one datacube. We impose a regular grid with $1''.6 \times 1''.6$ large pixels and calculate the areal overlap between all circular fiber apertures and the pixels. The flux in each fiber is then distributed to pixels according to the overlap.

Finally, we spatially rebin the final datacube to increase the observed signal-to-noise ratio (S/N) using the implementation for Voronoi Tessellation by Cappellari & Copin (2003).

3. Analysis: kinematics, photometry, and stellar populations

In this Section, we measure the stellar and ionized gas kinematics of NGC 4191 and its structural components. The stellar library we use is presented in Section 3.1. We first analyze the spectra with a non-parametric fit to recover the shape of the line-of-sight velocity distribution (LOSVD) in each spatial bin (Section 3.2). Motivated by the bimodality of the recovered LOSVDs, we apply a spectral decomposition technique to investigate and characterize the presence of two kinematically distinct stellar components (Section 3.3). In Sect. 3.3, we also study the structural components of NGC 4191 and investigate the connection between the photometric and kinematics components. We then measure the properties of stellar populations of the two kinematic components: line strength indices, age, metallicity, and abundance ratios of α elements (Section 3.4). The distribution of the ionized gas is discussed in Section 3.5.

3.1. The stellar library

The stellar library used in the spectroscopic fit consists of 12 stars observed with Virus-W using the same observational set-up of the galaxy observations. This ensures that the stellar templates had the same line spread function of the galaxy, minimizing systematic effects due to mismatch between the resolution of the stars and the galaxy spectra. This is particularly important for systems with low velocity dispersion, where the asymmetries in the LOSVDs are comparable with asymmetries in the line spread function.

The selected stars covered a large range of the $H\beta$, $Mg\ b$, $[MgFe]'$, and $\langle Fe \rangle$ parameters space, as shown in Figure 1.

3.2. Shape of the line-of-sight velocity distributions

We fitted the spectra with a non-parametric approach in order to recover the shape of the LOSVDs and investigate the presence of multiple kinematic components. The fitting procedure is described in Fabricius et al. (2014), and it extends the maximum penalized likelihood method by Gebhardt et al. (2000) to treat nebular emissions. After fitting and removing the continuum with a 3-rd degree polynomial, we fitted the wavelength range from 4905 \AA – 5325 \AA . We modeled the LOSVD with 31 independent velocity channels and linearly combined the set of 12 stellar spectra from a library (Sect. 3.1). We successively re-

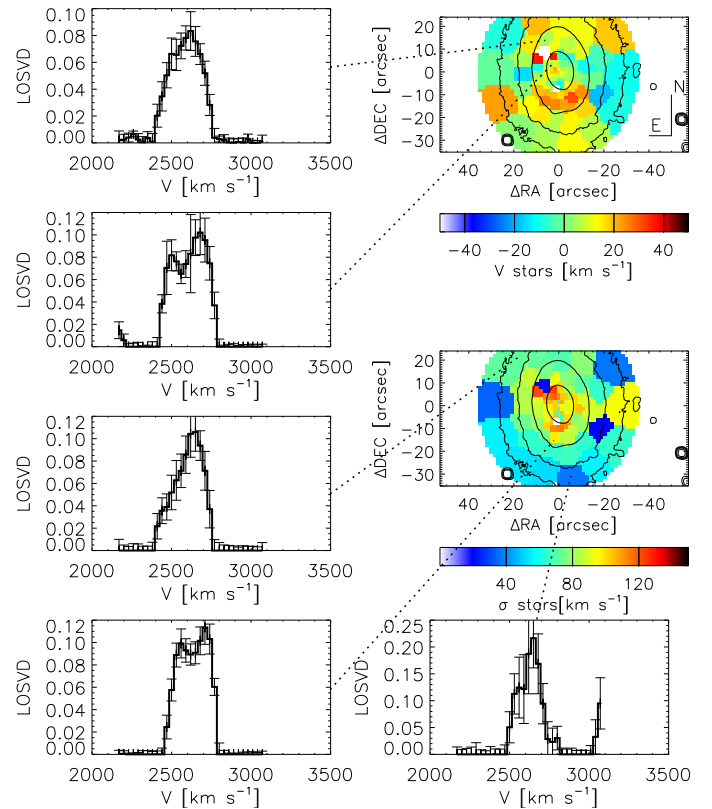


Fig. 2. Best fit kinematics for the single stellar component model. The two-dimensional maps show the velocity and velocity dispersion fields. The plots on the side show some example of reconstructed non-parametric LOSVDs in the location of the field of view indicated by the dotted lines. The LOSVDs of central regions clearly show a bimodal distribution; the LOSVDs in the outer regions show high asymmetry, which can be due to the presence of an unresolved secondary kinematic component.

moved stellar spectra that received small weights. The final fit was carried out with six templates. Due to the high S/N of the data after binning (typically 90 per \AA) we did not employ any penalization. For a number of bins the derived LOSVDs show a clear bimodal structure expressed as a double peak.

These bifurcated LOSVDs are more evident in the inner regions of the galaxies ($r < 10''$) and are spatially consistent with the regions where the sigma-peaks were detected. For the regions outside $10''$ the LOSVDs are strongly asymmetric, consistent with the interpretation that the galaxy contains two counter-rotating stellar components.

Figure 2 shows the shape of the LOSVDs in some spatial bins. In order to measure the mean kinematics along the line-of-sight, we re-fitted the spectra parametrizing the LOSVD in each bin with Gaussian function plus high-order Gauss-Hermite moments. The fit was done using a modified version of the Penalized Pixel Fitting code of Cappellari & Emsellem (2004) that included simultaneous fits to the ionized gas emission lines. Fig. 2 shows the velocity and velocity dispersion fields obtained with the parametric fit. The two peaks in the velocity dispersion profile discovered by Krajnović et al. (2011) are visible, slightly offset by $\approx 1''$ towards South East with respect to the galaxy photometric major axis. The velocity field is complex and it is not consistent with a single rotating component, even if high-order moments are taken into account in the LOSVD parametriza-

tion, providing further support to the presence of kinematically decoupled components.

3.3. Kinematics and photometry of the counter-rotating stellar components

Driven by the results of Section 3.2, we apply a spectral decomposition technique to investigate and characterize the presence of two kinematically distinct stellar components.

The spectral decomposition, described in Section 3.3.1, returns for each spatial bin the kinematics, the spectra, and the normalized flux contribution of the two stellar components. We also fit the intensities of the emission lines, and their mean velocity and velocity dispersion. We used the same spectral library for both the components, and let the code to select the most appropriate stellar template for each of them.

In Section 3.3.2 we associate these two kinematic components with the galaxy structural components derived from a photometric decomposition.

3.3.1. Spectral decomposition technique

The parametric fit of the stellar kinematics and the separation of two kinematic stellar components is done using the spectral decomposition technique developed in Coccato et al. (2011), implemented as modification to the Penalized Pixel Fitting code (Cappellari & Emsellem 2004).

The technique builds two optimal templates by linear combination of stellar spectra from an input library (see Section 3.1). The two templates are convolved with two independent LOSVDs, which are parametrized by two independent Gaussian functions. The convolved templates are then multiplied by Legendre polynomials to account for the shape of the continuum. Our implementation includes Gaussian functions that are added to fit the ionized gas emission lines $H\beta$ and $[O III] \lambda\lambda 4959, 5007\text{\AA}$. The best fit model is recovered using the Levenberg-Marquadt χ^2 minimization. The procedure allows the flux of the two components either to be free parameters in the fit or to be constrained to specified values or within a certain range. The code returns the best fit values for the stellar kinematics and the best fit spectra of the two stellar components, which will be used in Section 3.4 to derive their stellar populations. Also, the code returns the light contribution of one component relative to the total galaxy spectrum. If we label the two components with “A” and “B”, the code returns $F_A = \frac{I_A}{I_A + I_B}$, where I_A and I_B are the flux of the two components. By construction, $F_B = 1 - F_A$.

Our technique has been successfully applied to disentangle counter-rotating stellar disks in galaxies (Coccato et al. 2011, 2013; Pizzella et al. 2014), stars from the bulge and disk (Fabricius et al. 2014), and stars from the host galaxy and the surrounding polar disk (Coccato et al. 2014).

For the special case of NGC 4191, in order to obtain a reasonable and stable fit, it is necessary to constrain the flux ratio of the two kinematic components by performing an independent photometric decomposition (Section 3.3.2). This is due to a degeneracy between the parameters that describe the kinematics and the stellar populations of the two components. The same approach has been adopted in Katkov & Chilingarian (2011) and Coccato et al. (2014).

3.3.2. Photometric constraints

The aim of this section is to perform a photometric decomposition of NGC 4191 in order to constrain the flux parameter F_A in the spectral decomposition code.

We acquired a g -band image (the closest match to the VIRUS-W wavelength range) from the SDSS DR7 archive and analyzed it using the 2D image-fitting code IMFIT (Erwin 2015). The fitting procedure includes the convolution for a Moffat point spread function (PSF) computed using the median FWHM and β values measured from stars in the same image.

The best fit model is obtained adopting three components: a bulge with Sérsic profile, one inner exponential disk, and one outer exponential disk. In the fitting procedure, the center has been kept fixed for all the 3 components. The position angle and the ellipticity of the three components are independent, but constant with radius.

The structural parameters of the best fitting components are given in Table 1, and the best fit model is shown in Figures 3 and 4. The residual map of Fig. 3 highlights a spiral-arm pattern, indicating the presence of faint spiral arms and dust in this galaxy, despite of its classification as S0.

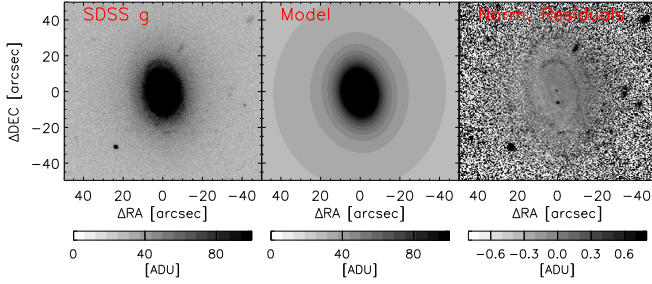
Our photometric decomposition represents an improvement of the previous single component model by Krajnović et al. 2013. One way to evaluate the *relative* goodness-of-fit of different models to the same data is via information-theoretic measures such as the Akaike Information Criterion (AIC) or Bayesian Information Criterion (BIC), both of which are output by IMFIT at the end of the fitting process. Unlike the χ^2 statistic, AIC and BIC do not require that models being compared be nested. The absolute values of these statistics are irrelevant; what matters is the relative value, with lower values indicating a better match to the data. Traditionally, $\Delta AIC = AIC_1 - AIC_2 < -10$ is taken as an indication for the clear superiority of model 1 over model 2. We find that the Sérsic + two exponential model is clearly favored. In the case of the g -band image, the three-component model has $\Delta AIC = -1442$ compared to the Sérsic + single-exponential model and $\Delta AIC = -15006$ compared to the single-Sérsic model. The values for the BIC are similarly large: $\Delta BIC = -1398$ and -14919 , respectively.

Figure 5 provides additional support to the choice of three-components model over one- or two- components models. It shows the radial profiles of ellipticity and position angle as measured from the g -band image and from the various models. We can see that the single-Sérsic model does a particularly poor job of reproducing the position angle radial variation, and the two-components model does not reproduce the change of ellipticity as nicely as the three-components model for $25'' < a < 30''$ and $a > 45''$. For use in constraining the flux parameter F in the spectral decomposition, we therefore use the three-components model.

We define “main kinematic component” the sum of the bulge and outer disk and “secondary kinematic component” the inner disk. The main kinematic components contains the $\sim 64\%$ of the total galaxy luminosity, whereas the secondary kinematic component contains the $\sim 36\%$ of the total galaxy luminosity. The particular association of the inner disk component with the counter rotating kinematic component is driven by its relative local luminosity. From the observed peaks in the LOSVDs we know that the two components have flux ratios between 1:3 and 1:1. Other combinations, such as defining the secondary component as the sum of the two disks, would have set one of the components below a detection limit ($F < 0.15$, see Appendix A), which is inconsistent with the observations.

Table 1. Best fit parameters of the photometric decomposition of NGC 4191.

| Sérsic bulge | | | |
|------------------------|-------|-------------|-----------------------------|
| PA | 13.3 | ± 0.7 | [degrees] |
| ell | 0.128 | ± 0.003 | |
| n | 2.87 | ± 0.06 | |
| μ_e | 19.7 | ± 0.05 | [mag arcsec ⁻²] |
| r_e | 2.22 | ± 0.07 | [arcsec] |
| m_{TOT} | 14.89 | ± 0.05 | [mag] |
| Inner exponential disk | | | |
| PA | 7.8 | ± 0.1 | [degrees] |
| ell | 0.384 | ± 0.003 | |
| μ_0 | 19.78 | ± 0.02 | [mag arcsec ⁻²] |
| h | 6.54 | ± 0.05 | [arcsec] |
| m_{TOT} | 14.23 | ± 0.02 | [mag] |
| Outer exponential disk | | | |
| PA | -2.7 | ± 0.7 | [degrees] |
| ell | 0.189 | ± 0.004 | |
| μ_0 | 22.26 | ± 0.01 | [mag arcsec ⁻²] |
| h | 20.9 | ± 0.1 | [arcsec] |
| m_{TOT} | 14.02 | ± 0.01 | [mag] |

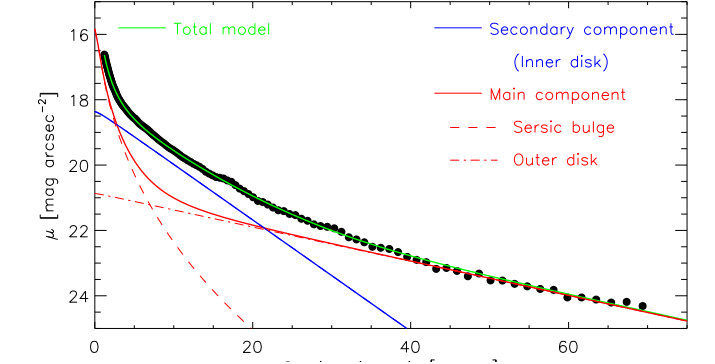
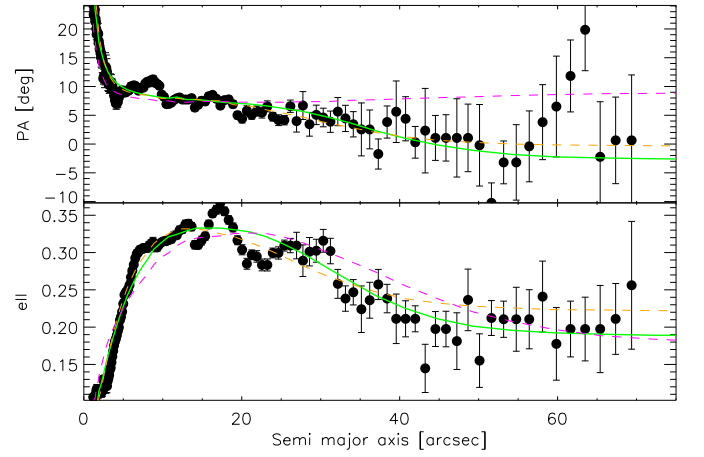

Fig. 3. Result of the photometric decomposition of NGC 4191. Left panel: SDSS *g* image; central panel: best fit model; right panel: normalized residuals (data - model)/model. North is up and East is left.

At each position (x, y) in the field of view, we can define the fraction of galaxy surface brightness contributed by the main and secondary components as:

$$\begin{aligned}
 F_{\text{main}}(x, y) &= F_A = \frac{I_{\text{main}}(x, y)}{I_{\text{main}}(x, y) + I_{\text{second}}(x, y)} \\
 &= \frac{I_{\text{bulge}}(x, y) + I_{\text{outer disk}}(x, y)}{I_{\text{bulge}}(x, y) + I_{\text{outer disk}}(x, y) + I_{\text{inner disk}}(x, y)} \\
 F_{\text{second}}(x, y) &= F_B = \frac{I_{\text{second}}(x, y)}{I_{\text{main}}(x, y) + I_{\text{second}}(x, y)} \\
 &= \frac{I_{\text{inner disk}}(x, y)}{I_{\text{bulge}}(x, y) + I_{\text{outer disk}}(x, y) + I_{\text{inner disk}}(x, y)} \\
 &= 1 - F_{\text{main}}(x, y)
 \end{aligned}
 \tag{1}$$

In Figure 6 we show the radial trend along the major axis of F_{second} .

The results of the photometric decomposition can be now used to constrain the spectral decomposition analysis. For a given spatial bin, we constrain the parameter F_A in the spectral decomposition code to be within the range $F_{\text{main}} - 0.05 < F_A < F_{\text{main}} + 0.05$; F_{main} is given by:


Fig. 4. Results of the photometric decomposition. Filled circles: surface brightness radial profile measured on the SDSS *g*-band image with the iraf task ellipse. The blue curve is the best fitting inner disk component, the red-dashed curve is the best fitting Sérsic bulge, and the red dot-dashed curve is the outer disk component. The green curve is the sum of all the best fitting components. Red and blue curves represent the profiles of the adopted definition for the main and secondary kinematics components, respectively.

Fig. 5. Comparison between the radial profile of ellipticity (top panel) and position angle (bottom panel) obtained with different photometric models. Filled circles: surface brightness radial profile measured on the SDSS *g*-band image with the iraf task ellipse. Green line: three-components model; orange dashed line: two-components model; magenta dashed line: single-component model.

$F_{\text{main}} + 0.05$; F_{main} is given by:

$$F_{\text{main}} = \frac{\sum I_{\text{main}}(x, y)}{\sum I_{\text{main}}(x, y) + \sum I_{\text{second}}(x, y)}$$

where the sum is done over all the spaxels contributing to a given spatial bin.

3.3.3. Kinematics of the counter-rotating stellar components

Figure 7 shows the kinematics of the two stellar components, as obtained from the spectral decomposition fit.

The main galaxy component, which consists in the combination of the Sérsic bulge and the large-scale exponential disk, is more luminous. It is characterized by a rotation amplitude of $\sim 70 \text{ km s}^{-1}$, with some scatter, and an average velocity dispersion of $\sim 120 \text{ km s}^{-1}$.

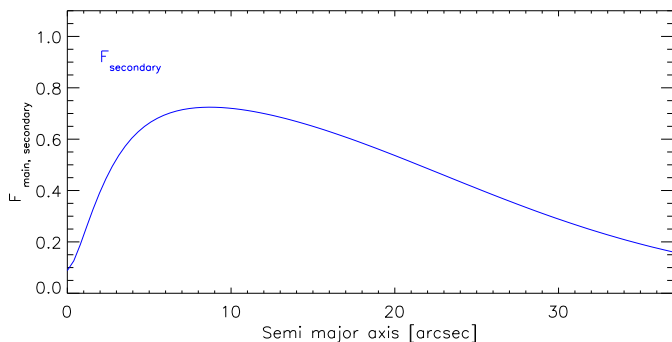


Fig. 6. Radial profiles of the relative flux contribution of the secondary stellar components $F_{\text{secondary}}$. The contribution of the main component is $F_{\text{main}} = 1 - F_{\text{secondary}}$ by construction.

The secondary galaxy component, which is represented by the inner exponential disk, is less luminous and it counter-rotates with respect the main stellar component. It has a rotation amplitude of $\sim 130 \text{ km s}^{-1}$ and an average velocity dispersion of $\sim 90 \text{ km s}^{-1}$. The direction of rotation is aligned with that of the ionized gas.

As additional test, we have performed the spectral decomposition using the constraints from the two-components photometric model. Although the main kinematic results are consistent with those presented above, the two-dimensional kinematic maps obtained with the two-components photometric model have higher noise. This is due to the poorer quality of the photometric fit, which translates into larger uncertainty in constraining the light content of the counter-rotating stellar components.

3.4. Stellar populations of the counter-rotating stellar components

We measured the $H\beta$, $Mg\ b$, $Fe5270$, and $Fe5335$ line-strength indices on the optimal template of each stellar component returned by the spectral decomposition code. The spectra are broadened with a Gaussian function to match the spectral resolution of the Lick system (8.4 \AA , Worthey & Ottaviani 1997). Therefore, we obtained two sets of indices in each spatial bin, one set for each kinematic component.

Measurements were scaled to the Lick system by comparing the line strength indices measured in the spectra Lick standard stars HD102870 and HD125560 obtained with VIRUS-W with those published by Worthey et al. (1994). The offsets are $-0.35 \pm 0.13 \text{ \AA}$ ($H\beta$), $-0.05 \pm 0.01 \text{ \AA}$ ($Mg\ b$), $-0.02 \pm 0.15 \text{ \AA}$ ($Fe5270$), and $-0.06 \pm 0.12 \text{ \AA}$ ($Fe5270$). We applied this correction to the $H\beta$ and $Mg\ b$ indices, but not for the metal indices, because they are negligible considering the measurements errors.

In Figure 8, we show the combined indices $H\beta$, $Mg\ b$ [$MgFe$], and $\langle Fe \rangle$ of the two stellar components. The scatter in the plots is large, reflecting the uncertainties in our measurements. In particular, we note that the scatter in the measurements in the $Mg\ b$ $\langle Fe \rangle$ plane of Fig. 8 is larger for the secondary component. This is probably due to a combined effect of i) radial gradients that are more pronounced for the secondary component (see below); and ii) secondary component being on average the less luminous, and therefore the errors in the measurements are larger.

Fig. 8 also compares our measurements to the predictions of stellar population models (Thomas et al. 2003). This allows us to derive their two-dimensional maps of age, metallicity, and

abundance ratios of α elements, which are shown in Figure 9. Figs. 8 and 9 do not show the results on those spatial bins where the S/N is lower than 25 per \AA . In Fig. 9 we also compute median values within elliptical annuli to highlight the presence of radial gradients in the properties of the stellar populations. The error in each elliptical bin is computed as the maximum between i) the scatter of the measurements within that elliptical bin, and ii) the weighted mean error $1/\sqrt{\sum_i 1/\sigma_i^2}$, where σ_i are the individual measurements errors in age, $[Z/H]$, and $[\alpha/Fe]$.

The properties of the stellar populations of the two counter-rotating stellar components are very similar, as shown by Figs. 8 and 9. Because the scatter in the two-dimensional maps is large and a direct comparison is difficult, we compare average quantities. Metallicities and abundances of α elements are consistent with solar, without significant radial gradients. Their mean values are: $\langle [Z/H] \rangle_{\text{main}} = 0.02 \pm 0.09 \text{ dex}$, $\langle [Z/H] \rangle_{\text{second}} = -0.1 \pm 0.2 \text{ dex}$, $\langle [\alpha/Fe] \rangle_{\text{main}} = -0.05 \pm 0.05 \text{ dex}$, and $\langle [\alpha/Fe] \rangle_{\text{second}} = -0.02 \pm 0.05 \text{ dex}$. On the other hand, the age radial profiles show a mild indication of radial gradients. The age of the stars in the main component ranges from $\sim 12 \text{ Gyr}$ in the central regions down to $\sim 6 \text{ Gyr}$ at $21''$. Outside $21''$ the age rises again, but the uncertainties at these radii become too large to derive conclusive results. One possible explanation is that, if the observed raise in age is real, it might be due to accretion of old stars, which were accreted in the same rotation direction as the main component. The age of the stars in the secondary component ranges from $\sim 12 \text{ Gyr}$ in the central regions down to $\sim 3 \text{ Gyr}$ at $21''$, remaining nearly constant afterwards. We compare the mean ages of the two components within $21''$, which can be considered the upper limit for trusting age measurements in the main component. We find: $\langle \text{age} \rangle_{\text{main}}(R < 21'') = 10 \pm 3 \text{ Gyr}$ and $\langle \text{age} \rangle_{\text{second}}(R < 21'') = 5 \pm 4 \text{ Gyr}$. The mean ages of the two stellar components agree within the errorbars; on the other hand, the radial profiles in Fig. 9 seem to indicate that the secondary component is systematically younger than the main galaxy by $\approx 2 \text{ Gyr}$ at all radial bins. Implications of this age difference, if real, will be discussed in Section 4.

By comparing the mean properties of the stellar populations with the model predictions by Maraston (2005) assuming a Salpeter initial mass function, we can derive the mean values of the stellar mass-to-light ratios of the two components in the g band: $\langle M/L_* \rangle_{\text{main}} = 6.7 \pm 2.5$, $\langle M/L_* \rangle_{\text{second}} = 3.3 \pm 2.5$. These informations, combined with the luminosity of the two components measured in Sect. 3.3.2 and the adopted distance of 42.4 Mpc , allow us to estimate their masses: $M_{\text{main}} = 6.2 \pm 2.3 \cdot 10^{10} M_{\odot}$ and $M_{\text{second}} = 1.0 \pm 9.4 \cdot 10^{10} M_{\odot}$; the main stellar component is ≈ 6 times more massive than the secondary component.

3.5. Kinematics and distribution of the ionized gas

The spectral decomposition routine fits also the ionized gas emission lines. The gas component (see Fig. 7) rotates along the same direction of the secondary stellar component with an amplitude of $\sim 150 \text{ km s}^{-1}$. The velocity dispersion decreases with radius: from $\sim 60 \text{ km s}^{-1}$ in the center down to $\sim 30 \text{ km s}^{-1}$ in the outskirts. The high value of velocity dispersion measured in the inner $1''$ ($\sim 100 \text{ km s}^{-1}$) is probably due to the seeing and the limited spatial resolution.

The emission lines are very weak, therefore it was necessary to spatially bin the data to measure their kinematics as in the case of the stars. For convenience, we adopted the same spatial binning as for the stellar component to measure the gas kinematics. However, this ‘‘coarse’’ binning, prevents us to inves-

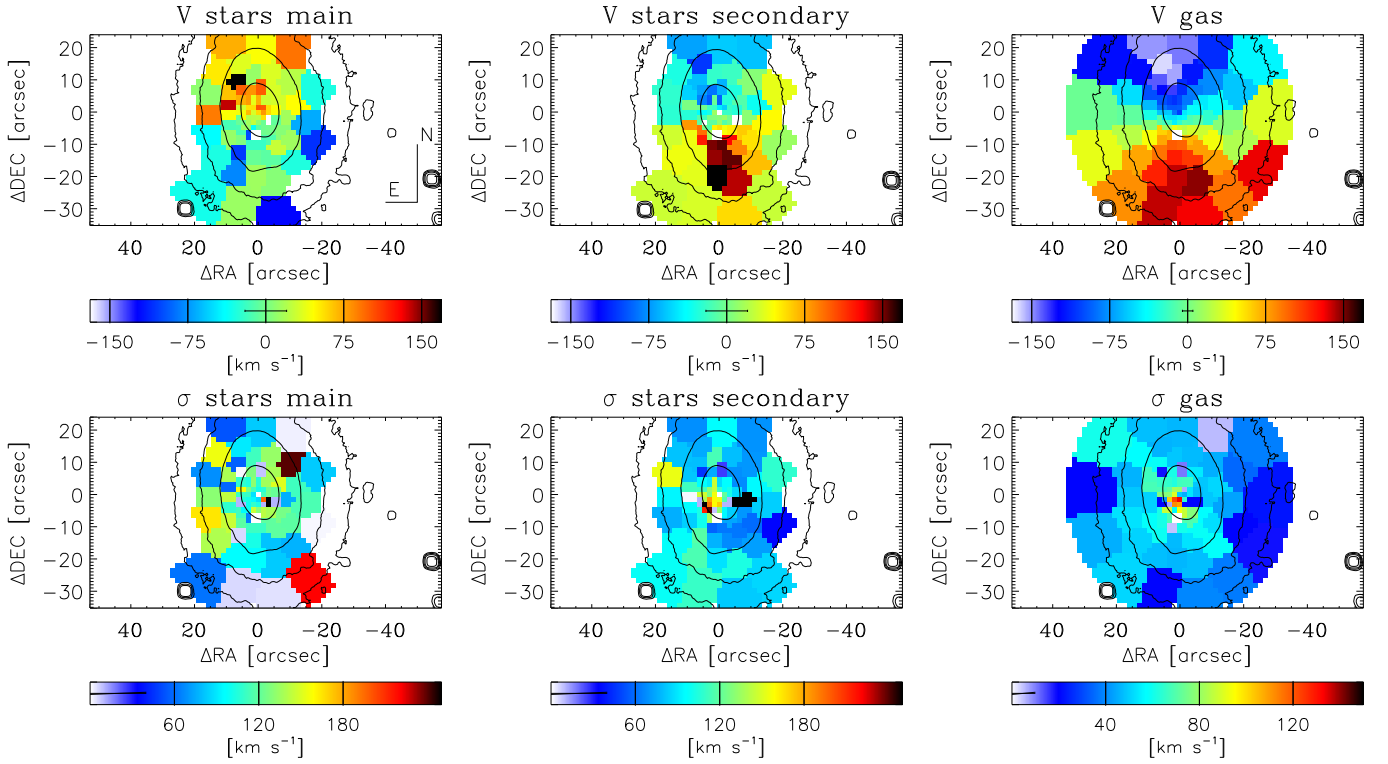


Fig. 7. Result of the spectral decomposition of NGC 4191. Velocity (top panels) and velocity dispersion (bottom panels) maps for the main stellar component (left panels), secondary counter-rotating stellar component (central panels) and counter-rotating ionized-gas component (right panels) are shown. Spatial bins with S/N lower than 25 per \AA are not shown for the stellar components. The horizontal bars in the color scale at the bottom of each panel indicate the mean error.

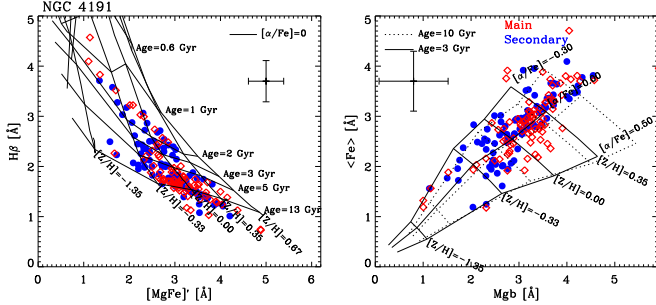


Fig. 8. Line strength indices of the two counter-rotating stellar components in NGC 4191. Blue filled circles and red open diamonds refer to the main and secondary component, respectively. The error bars represent the mean errors in the measurements. The line grids represent the predictions of simple stellar population models (Thomas et al. 2003). Spatial bins with S/N lower than 25 per \AA are not considered.

tigate the spatial distribution of the emission lines. We therefore re-analyzed the gas distribution on a finer spatial grid and measured the equivalent widths of the $H\beta$ [O III] $\lambda 4959$, and [O III] $\lambda 5007\text{\AA}$ emission lines on this latter spatial binning.

Figure 10 shows the spatial distribution of the [O III] $\lambda 5007\text{\AA}$ emission line equivalent widths, which is the most intense. Although the outer regions are dominated by the noise due to lower signal-to-noise of the data, an elongated ring-like structure (or maybe a spiral arm structure) with three blobs is visible within $25''$. The position angle of the structure, using the two brightest blobs in the equivalent width map as reference, is 8.0° , which is

very close to the position angle of the secondary component, i.e. 7.8° (Table 1). This strengthens the association of the ionized-gas component to the secondary stellar component.

Interestingly, a similar spiral-like structure with same size and orientation, is observed in the residual map of Fig. 3, consistently with the concentration of gas along spiral arms. Unfortunately, the spatial binning we adopted for the stellar population studies does not have enough spatial resolution to resolve the spiral arms and separate their stellar population from that of the rest of the galaxy.

It is interesting to compare, although qualitatively, the distribution of emission lines of NGC 4191 with those of other stellar counter-rotating galaxies studied so far. The distribution of the ionized gas in NGC 4191 resembles those of NGC 3593 and NGC 5719, where the gas is also distributed along a ring-like structure with presence of blobs. In addition, in the case of NGC 5719, the location of the most intense blobs coincides with that of the youngest stars. In the case of NGC 4550, the gas has irregular distribution, with no signature of ring-like or spiral-like structures. Also, NGC 4550 is the galaxy where the two stellar components are the oldest.

4. Discussion and conclusions

The LOSVD of NGC 4191 are complex and suggest the presence of two kinematically-decoupled stellar components. Their properties have been investigated with the aid of a non-parametric fit (Fabricius et al. 2014) and a spectral decomposition technique (Coccato et al. 2011).

We also performed a parametric photometric decomposition of the surface-brightness distribution of NGC 4191. Our detailed

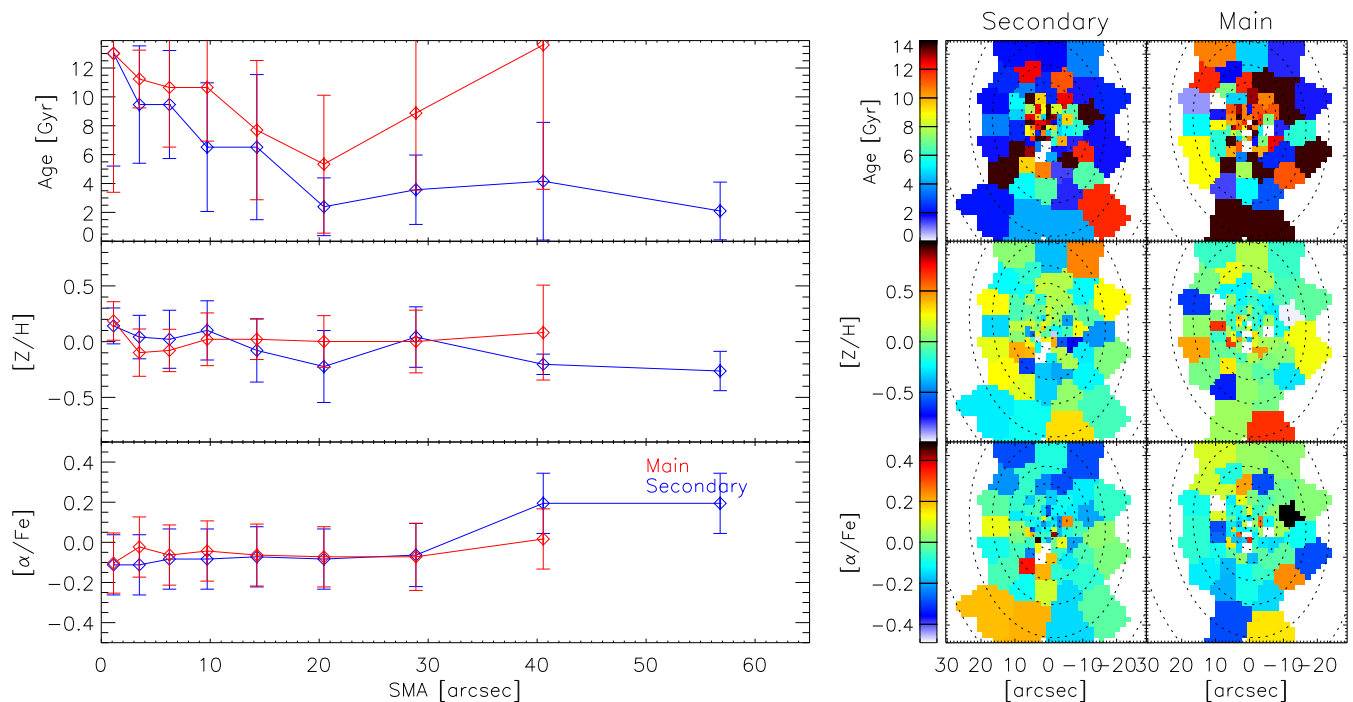


Fig. 9. Properties of the stellar populations of the counter-rotating components in NGC 4191. Left panels: median values of age (top panel), $[Z/H]$ (middle panel) and $[\alpha/Fe]$ (bottom panel) within elliptical annuli for the main (red line) and secondary (blue line) stellar components. Right panels: two dimensional maps of the stellar population properties. The dashed lines indicate the elliptical annuli used in the computation of the median values presented in the left panels. Spatial bins with S/N lower than 25 per \AA are not considered in the analysis.

analysis reveals the presence of three structural components, which were overlooked in previous studies: a Sérsic bulge and two exponential disks of different scale lengths. Also, faint spiral structures (stars and dust) are visible from the residual map.

We then linked the photometric components to the kinematic components unveiled by the spectroscopic analysis. The intensity of the double peaks in the LOSVDs allowed us to associate the bulge and the outer exponential disk with the main kinematic component. Together they represent the $\sim 64\%$ of the total galaxy luminosity. Consequentially, we associated the inner exponential disk with the secondary kinematic component, which represents the $\sim 36\%$ of the total galaxy light.

The information on the photometry allowed us to constrain the relative light contribution of the two kinematic components in the spectral decomposition fit. This decreases the degeneracy between the various fitting parameters that characterize the two components (kinematics, surface brightness, and stellar populations) and allows us to obtain a more reliable fit.

We find evidences that the two kinematic components in NGC 4191 counter-rotate with respect to each other. The secondary component rotates faster and along the same direction as the ionized gas. The main component rotates slower and it has higher velocity dispersion, consistent with hosting also bulge stars.

The properties of the stellar populations of the two kinematic components are very similar, although the large uncertainties in the measurements prevent us to make strong claims. We have azimuthally averaged the measurements onto elliptical bins to reduce the statistical noise and highlight the presence of radial gradients. Fig. 9 gives a tentative indication that the luminosity-weighted ages of the stars in the secondary disk are systematically lower than those of the main components at all radii. We

can explain the age difference between the two components with the following scenario.

The combination of kinematics and stellar populations gives us clues on the formation mechanism of NGC 4191. Our data favor the scenario in which a disk galaxy (represented by the main kinematic component, i.e., the bulge plus the outer disk) acquired material (either gas/stars accretion or galaxy mergers) from the outside onto retrograde orbit, which formed the counter-rotating secondary component. At first glance, this scenario is the same of those of the other counter-rotating systems studied so far (Coccato et al. 2011, 2013; Katkov et al. 2013; Pizzella et al. 2014). However, there are some important differences between NGC 4191 and these other galaxies.

First, the age radial gradients observed in NGC 4191 are much steeper than those observed in other systems. Moreover, the age gradient of the secondary component is negative, whereas in the other systems is positive. This is indicative of an inside-out star formation process for the secondary disk, and favors the gas accretion scenario over major merger. A nearly 1:1 merger in fact would have redistributed the stars along all directions, smoothing any significant age gradient.

Second, there are almost no differences in the metallicity and α -elements overabundance ratio between main and secondary components, whereas differences were observed in other galaxies. In other galaxies, the scenario that better explained the differences in $[Z/H]$ and $[\alpha/Fe]$ between the main and secondary components is gas accretion from cosmic gas reservoir or from a nearby gas-rich companion. The case of NGC 5719 offers the best example of such a scenario: we observe the on-going gas stripping process from its nearby companion that forms the counter-rotating stellar disk (Vergani et al. 2007; Coccato et al. 2011). On the contrary, the data for NGC 4191 suggest that the

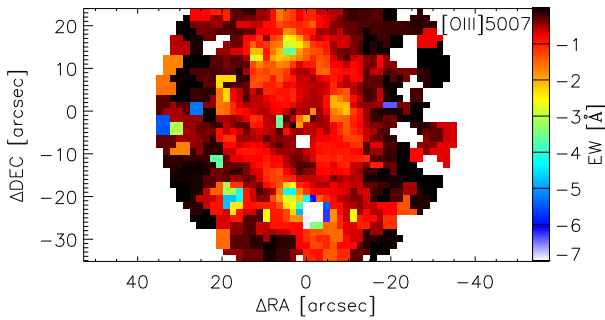


Fig. 10. Distribution of the [O III] $\lambda 5007\text{\AA}$ emission line. The gas is distributed on a ring-like structure aligned with the photometric major axis of the secondary component (see text for details).

accreted gas has origin in common with the gas that formed the main galaxy component.

The observed properties of NGC 4191 can be interpreted in light of cosmological simulations (Algorry et al. 2014). The main galaxy component is formed via accretion of gas from two filaments that have very similar chemical composition. As time passes, each filament torques the other in opposite direction, resulting into a “double accretion” with opposite spin. Initially, the accretion from the two filaments occur at the same time. The collisional nature of the gas ensures that only one stellar component forms, from gas whose properties is a mixture of that of the two filaments, and with the spin dictated by the most massive filament. After a while (~ 2 Gyr, considering the measured age difference between the two components in each radial bin), the accretion along one of the filaments stops.

The accretion process continues along the counter-rotating filament, which wipes out the remaining gas and forms the secondary counter-rotating component. The star formation occurs inside-out, as suggested from the negative age gradient; the new born stars have properties very similar to those of the main component, because the gas is a mixture of that of the second filament and what remained from the first filament. Moreover, the formation of the secondary component must have occurred right after the formation of the main component and very rapidly, without leaving the stars of the first component enough time to reprocess and enrich the gas with metals and/or α elements. This is consistent with the relative small age difference between the two components and their equal and constant $[Z/H]$ and $[\alpha/Fe]$ radial profiles. The rapid star formation process and the solar abundances and metallicity measured for the stellar populations, imply that the infalling gas was already enriched, because otherwise there would not be enough time to reach the measured values of $[Z/H]$ and $[\alpha/Fe]$.

The hypothesis where the main component formed first is consistent with the observed properties of the photometric components: the position angles are slightly different and the ellipticities of the Sérsic bulge and outer disk are smaller than that of the secondary component (inner disk, see Tab. 1). The most likely interpretation is that the bulge is triaxial and the disks have different thickness (the external disk being the thickest). This is in agreement with the proposed formation scenario: the main component formed first and had more time to heat up its disk during the accretion of the gas that originated the secondary component. Gas accretion can indeed heat the host stellar disk during the formation of a counter-rotating component (i.e., Thakar & Ryden 1996).

To conclude, we would like to remark the importance of disentangling and measuring the properties of individual components in multi-spin galaxies to understand their formation mechanisms. Also, the special case of NGC 4191 supports the validity of the double peaked signature in the velocity dispersion field associated to zero-velocity rotation as selection criteria for identifying counter-rotating galaxies. This is very useful for large integral field spectroscopic surveys to provide a statistically completed census of counter-rotating galaxies in the nearby universe.

References

- Algorry, D. G., Navarro, J. F., Abadi, M. G., et al. 2014, *MNRAS*, 437, 3596
 Bertola, F., Buson, L. M., & Zeilinger, W. W. 1992, *ApJ*, 401, L79
 Bryant, J. J., Owers, M. S., Robotham, A. S. G., et al. 2015, *MNRAS*, 447, 2857
 Bundy, K., Bershady, M. A., Law, D. R., et al. 2015, *ApJ*, 798, 7
 Cappellari, M. & Copin, Y. 2003, *MNRAS*, 342, 345
 Cappellari, M. & Emsellem, E. 2004, *PASP*, 116, 138
 Cappellari, M., Emsellem, E., Krajnović, D., et al. 2011, *MNRAS*, 413, 813
 Coccato, L., Iodice, E., & Arnaboldi, M. 2014, *A&A*, 569, A83
 Coccato, L., Morelli, L., Corsini, E. M., et al. 2011, *MNRAS*, 412, L113
 Coccato, L., Morelli, L., Pizzella, A., et al. 2013, *A&A*, 549, A3
 Corsini, E. M. 2014, in *Astronomical Society of the Pacific Conference Series*, Vol. 486, *Multi-Spin Galaxies*, ASP Conference Series, ed. E. Iodice & E. M. Corsini, 51
 Crocker, A. F., Jeong, H., Komugi, S., et al. 2009, *MNRAS*, 393, 1255
 de Zeeuw, P. T., Bureau, M., Emsellem, E., et al. 2002, *MNRAS*, 329, 513
 Erwin, P. 2015, *ApJ*, 799, 226
 Evans, N. W. & Collett, J. L. 1994, *ApJ*, 420, L67
 Fabricius, M. H., Coccato, L., Bender, R., et al. 2014, *MNRAS*, 441, 2212
 Fabricius, M. H., Gruppi, F., Bender, R., et al. 2012, in *Society of Photo-Optical Instrumentation Engineers (SPIE) Conference Series*, Vol. 8446, *Society of Photo-Optical Instrumentation Engineers (SPIE) Conference Series*
 Fisher, D., Illingworth, G., & Franx, M. 1994, *AJ*, 107, 160
 Galletta, G. 1987, *ApJ*, 318, 531
 Gebhardt, K., Richstone, D., Kormendy, J., et al. 2000, *AJ*, 119, 1157
 Husemann, B., Kamann, S., Sandin, C., et al. 2012, *A&A*, 545, A137
 Johnston, E. J., Merrifield, M. R., Aragón-Salamanca, A., & Cappellari, M. 2013, *MNRAS*, 428, 1296
 Katkov, I. Y. & Chilingarian, I. V. 2011, *ArXiv*: 1111.5822
 Katkov, I. Y., Sil’chenko, O. K., & Afanasiev, V. L. 2013, *ApJ*, 769, 105
 Krajnović, D., Alatalo, K., Blitz, L., et al. 2013, *MNRAS*, 432, 1768
 Krajnović, D., Emsellem, E., Cappellari, M., et al. 2011, *MNRAS*, 414, 2923
 Maraston, C. 2005, *MNRAS*, 362, 799
 Pizzella, A., Corsini, E. M., Vega Beltrán, J. C., & Bertola, F. 2004, *A&A*, 424, 447
 Pizzella, A., Morelli, L., Corsini, E. M., et al. 2014, *A&A*, 570, A79
 Puerari, I. & Pfenniger, D. 2001, *Ap&SS*, 276, 909
 Rix, H.-W., Franx, M., Fisher, D., & Illingworth, G. 1992, *ApJ*, 400, L5
 Rubin, V. C., Graham, J. A., & Kenney, J. D. P. 1992, *ApJ*, 394, L9
 Sánchez, S. F., Kennicutt, R. C., Gil de Paz, A., et al. 2012, *A&A*, 538, A8
 Thakar, A. R. & Ryden, B. S. 1996, *ApJ*, 461, 55
 Theureau, G., Hanski, M. O., Coudreau, N., Hallet, N., & Martin, J.-M. 2007, *A&A*, 465, 71
 Thomas, D., Maraston, C., & Bender, R. 2003, *MNRAS*, 339, 897
 Vergani, D., Pizzella, A., Corsini, E. M., et al. 2007, *A&A*, 463, 883
 Worthey, G., Faber, S. M., Gonzalez, & et al. 1994, *ApJS*, 94, 687
 Worthey, G. & Ottaviani, D. L. 1997, *ApJS*, 111, 377

Appendix A: Errors of the spectroscopic decomposition

The ability of the spectral decomposition code to measure the kinematic and properties of the stellar populations depends on many parameters. First, on the differences of the two stellar components: the more separated they are in kinematics and stellar populations, the easier is to decouple their contribution from the observed galaxy spectrum. Also, the spectral resolution and wavelength range of the instrument and the signal-to-noise of the observations are important.

We therefore simulate galaxy spectra that represent observations and the instrumental set-up as close as possible. We then

perform the spectral decomposition on those simulated spectra to derive the errors on the measured quantities.

The simulated galaxy spectra are constructed by creating and adding two stellar templates broadened to have 100 km s^{-1} of velocity dispersion. The stellar templates are both constructed using the same star, HD106210, observed with the VIRUS-W (to match the instrumental set-up), that has line strength indices as close as possible to the mean measured values.

We then explore the parameters space defined by the velocity separation of the two component (ΔV), and the signal-to-noise ratio (S/N). For each point ($\Delta V, S/N$) in the parameter space we construct a set of 100 simulated galaxy spectra by adding Gaussian noise. We then perform the spectral decomposition on those simulated spectra to derive the errors on the measured quantities. The parameter space is sampled by $\Delta V = 50, 75, 100, 150, 250 \text{ km s}^{-1}$, and $\text{noise} = 0.005, 0.02, 0.03, 0.10$, that correspond to S/N ranging from 480 to 25 per \AA (the mean S/N of the binned spectra is 90 per \AA)².

We find that the errors on the absorption line indices does not vary much with velocity separation, because the stellar populations of the two components used in the simulations are the same (i.e. there is no degeneracy with the kinematics). There is also little dependence with S/N . The mean errors on the indices are 0.2 \AA , 0.4 \AA , 0.2 \AA , and 0.2 \AA , for the $H\beta$, $Mg b$, $Fe5270$, and $Fe5335$ indices, respectively.

We find that the errors on velocity separation between the two components depend on the input velocity separation and on the S/N . Figure A.1 shows the error on the recovered velocity separation as function of the input noise and input velocity separation. For typical values measured along the galaxy kinematic major axis, where the velocity separation is $\Delta V > 150 \text{ km s}^{-1}$ and the noise is $\text{rms} < 0.05$, the error on the velocity separation between the two components is $\approx 30 \text{ km s}^{-1}$. Also, the error on the recovered flux of the two components is $\sim 15\%$.

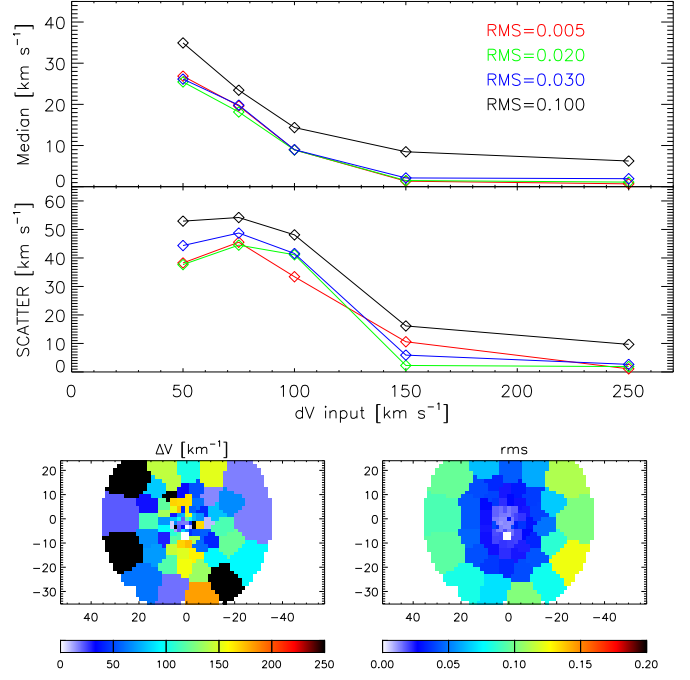


Fig. A.1. Top figure: median value (top panel) and standard deviation (bottom panel) of the error on the recovered velocities as function of the velocity difference between the two simulated stellar components. Different lines represent different signal-to-noise values per \AA : 480 ($\text{rms} = 0.005$), 120, 80, and 24 ($\text{rms} = 0.1$). Bottom figure: two-dimensional maps of the absolute velocity difference between the two stellar components (left panel) and the fit rms (right panel).

² We define the noise (rms) as the standard deviation of the residuals between the galaxy observed spectrum (normalized to its median value) and the best fit model. The actual computation on the wavelength region used in the fit and with the `robust_sigma` IDL routine. This value of rms is converted into a proxy for the S/N per angstrom by $S/N = 1/\text{rms}/\sqrt{0.178}$, where 0.178 is the inverse dispersion in \AA pixel^{-1} .